Image Cover Sheet

CLASSIFICATION	SYSTEM NUMBER
UNCLASSIFIED	152221

TITLE

MULTIPLE SCATTERING OF NARROW LIGHT BEAMS IN AEROSOLS

System Number:

Patron Number:

Requester:

Notes:

DSIS Use only:

Deliver to:

Appl. Phys. B 60, 315–323 (1995)

Applied Physics B Lasers and Optics

Multiple scattering of narrow light beams in aerosols

L. R. Bissonnette

DREV-Defence Research Establishment Valcartier, P.O. Box 8800, Courcelette, Québec, Canada G0A 1R0
(Fax: +1-418/844-4511, E-mail: LBISSON@sv0.drev.dnd.ca)

Received: 16 March 1994/Accepted: 29 March 1994

Abstract. A multiple scattering propagation model of narrow light beams in aerosol media is described. It is based on a paraxial approximation of the radiative transfer equation in which the flux normal to the incident beam direction is modeled by a diffusion process. The model solutions are the forward- and backscattered intensity profiles for the specified geometry and receiver aperture and field of view. The required inputs are the system parameters, and the aerosol single scattering angular phase function and extinction and scattering coefficients which are allowed to vary along the beam axis. Good agreement is shown with measurements performed in the laboratory over scales ranging from a few tens of mm to a few m, and in the atmosphere over a scale of the order of 1 km. The solutions are valid for optical depths smaller than ≈ 10, for phase functions corresponding to average size parameters of order one or greater, and for off-axis positions not exceeding $\approx 25\%$ of the reciprocal of the scattering coefficient.

PACS: 42.60

Light propagation in dense aerosol media is basically a multiple scattering problem. Depending on the aerosol parameters and the geometry of the application, the scattered radiation may contribute significantly to the transmitted and backscattered signals. It is important to be able to model these effects not only to take them into account when they affect the measurements but, possibly, to make use of the information they contain.

Various methods have been developed to calculate multiple scattering in particulate media. This special issue is a good collection of available models and a comparative study is made in a joint article [1]. The models of this issue are representative of the present state-of-the-art and fall under four main categories: numerical Monte Carlo calculations, stochastic description of photon scattering, solutions of Maxwell's equations, and approximations to the radiative transfer equation.

This paper describes an approximation to the radiative transfer equation applicable to the calculation of the forward- and backscattered radiation from narrow light beams. The solutions are obtained in general analytic formulas that require very modest computer resources for calculating the numerical results. They are valid in the paraxial approximation i.e., for observation points within a few degrees of the beam axis in both the forward and backward directions. The model was first described in [2] and solutions compared with measurements in [3, 4]. In this paper, a simplified derivation of the model is presented and the solutions for the most useful application geometries are compared with measurements derived from laboratory simulations and field experiments.

1 Proposed model

The problem of interest is well illustrated by the photograph in Fig. 1 of a HeNe laser beam propagating in turbid water. The photograph clearly shows that the unscattered narrow beam remains well defined far into the scattering medium but that it is surrounded by a halo which also has the geometry of a forward beam although much wider. It is this halo that we want to model along with its effects on backscatter.

The model is based on the time-independent radiative-transfer equation for the specific intensity $I(\mathbf{r}, \hat{\mathbf{s}})$, where $\mathbf{r}$ is the position vector and $\hat{\mathbf{s}}$ is the direction unit vector. The total $I(\mathbf{r}, \hat{\mathbf{s}})$ is written as the sum of the reduced- and diffuse-intensity components, $I_{ri}(\mathbf{r}, \hat{\mathbf{s}})$ and $I_d(\mathbf{r}, \hat{\mathbf{s}})$ respectively, i.e.,

$$I(\mathbf{r}, \hat{\mathbf{s}}) = I_{ri}(\mathbf{r}, \hat{\mathbf{s}}) + I_d(\mathbf{r}, \hat{\mathbf{s}}). \quad (1)$$

For the incident collimated beam geometry illustrated in Fig. 1, $I_{ri}(\mathbf{r}, \hat{\mathbf{s}})$ is given by

$$I_{ri}(\mathbf{r}, \hat{\mathbf{s}}) = I_0(z, \boldsymbol{\varrho})\, e^{-\tau}\, \delta(\omega - \omega_0), \quad (2)$$

where $I_0(z, \boldsymbol{\varrho})$ is the vacuum irradiance profile of the incident beam, $(z, \boldsymbol{\varrho})$ are the coordinates parallel and

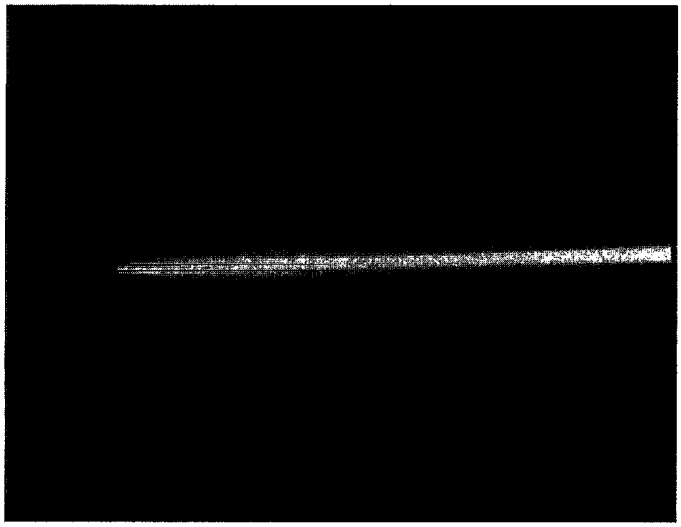

Fig. 1. Photograph of a HeNe laser beam propagating in turbid water

normal to the beam axis, ω and ω_0 are the solid angles about $\hat{\mathbf{s}}$ and $\hat{\mathbf{s}}_0$, $\hat{\mathbf{s}}_0$ is the direction of the incident beam, δ is the delta function such that $\int_{4\pi} d\omega\, \delta(\omega-\omega_0) = 1$, and τ is the optical depth. The time-independent radiative-transfer equation for the diffuse intensity I_d, given the incident beam of (2), is then

$$\nabla\cdot\hat{\mathbf{s}} I_d(\mathbf{r},\hat{\mathbf{s}}) + (\sigma_m+\sigma_e) I_d(\mathbf{r},\hat{\mathbf{s}}) = \frac{\sigma_s}{4\pi}\int_{4\pi} d\omega'\, P(\hat{\mathbf{s}},\hat{\mathbf{s}}')\, I_d(\mathbf{r},\hat{\mathbf{s}}') + \frac{\sigma_s}{4\pi} P(\hat{\mathbf{s}},\hat{\mathbf{s}}_0) \times I_0(z,\boldsymbol{\varrho})\exp(-\tau), \quad (3)$$

where σ_m is the molecular extinction coefficient of the medium, σ_e is the aerosol extinction coefficient, σ_s is the aerosol scattering coefficient, and $P(\hat{\mathbf{s}},\hat{\mathbf{s}}')$ is the aerosol single scattering angular phase function normalized such that

$$\frac{1}{4\pi}\int_{4\pi} P(\hat{\mathbf{s}},\hat{\mathbf{s}}')\, d\omega' = 1. \quad (4)$$

Integrating (3) successively over the forward and backward hemispheres defined about the direction $\hat{\mathbf{s}}_0$ of the unscattered beam, we obtain the following set of equations for the forward and backward flux

$$\mathbf{F}^{\pm} = \int_{(2\pi)^{\pm}} d\omega\, \hat{\mathbf{s}} I_d(\mathbf{r},\hat{\mathbf{s}}):$$

$$\nabla\cdot\mathbf{F}^{+} + (\sigma_m+\sigma_e) U_d^{+} = \frac{\sigma_s}{4\pi}\int_{(2\pi)^{+}} d\omega \int_{4\pi} d\omega'\, P(\hat{\mathbf{s}},\hat{\mathbf{s}}')\, I_d(\mathbf{r},\hat{\mathbf{s}}') + \sigma_s^{+} I_0(z,\boldsymbol{\varrho})\exp(-\tau), \quad (5)$$

$$\nabla\cdot\mathbf{F}^{-} + (\sigma_m+\sigma_e) U_d^{-} = \frac{\sigma_s}{4\pi}\int_{(2\pi)^{-}} d\omega \int_{4\pi} d\omega'\, P(\hat{\mathbf{s}},\hat{\mathbf{s}}')\, I_d(\mathbf{r},\hat{\mathbf{s}}') + \sigma_s^{-} I_0(z,\boldsymbol{\varrho})\exp(-\tau), \quad (6)$$

where

$$U_d^{\pm} = \int_{(2\pi)^{\pm}} d\omega\, I_d(\mathbf{r},\hat{\mathbf{s}}), \quad (7)$$

$$\sigma_s^{\pm} = \frac{\sigma_s}{4\pi}\int_{(2\pi)^{\pm}} d\omega\, P(\hat{\mathbf{s}},\hat{\mathbf{s}}_0). \quad (8)$$

Equations (5) and (6) constitute an integral but still exact form of the radiative transfer equation. The main difficulty with these equations comes from the integral scattering terms on the right-hand sides. To simplify these terms, we introduce a first hypothesis specific to the narrow beam geometry. We assume that, for narrow incident beams such as illustrated in Fig. 1 and for observation points $\mathbf{r}$ not too far from the beam axis, $I(\mathbf{r},\hat{\mathbf{s}})$ is peaked in the directions $\pm\hat{\mathbf{s}}_0$. This condition is not synonymous with the more common small-angle approximation, it is satisfied even for fairly broad single-scattering phase functions provided that the optical depth τ is not too large. Indeed, if τ is small enough, the major contributions to I_d originate from the narrow unscattered beam as shown in Fig. 1 and $I(\mathbf{r},\hat{\mathbf{s}})$ has maxima near 0° and 180° because it is there that the length of the unscattered beam seen per unit solid angle is the longest. The casual observer will confirm that a visible laser beam propagating in dusty air appears more intense when viewed at shallow angles, whether looking toward or away from the source. If $I(\mathbf{r},\hat{\mathbf{s}}')$ is peaked in the directions $\hat{\mathbf{s}}' = \pm\hat{\mathbf{s}}_0$, we can pull $P(\hat{\mathbf{s}},\hat{\mathbf{s}}')$ out of the integral over ω' and the first term on the right-hand side of (5) and (6) can be approximated as follows:

$$\begin{aligned}
&\frac{\sigma_s}{4\pi}\int_{(2\pi)^{\pm}} d\omega \int_{4\pi} d\omega'\, P(\hat{\mathbf{s}},\hat{\mathbf{s}}')\, I_d(\mathbf{r},\hat{\mathbf{s}}') \\
&\cong \frac{\sigma_s}{4\pi}\int_{(2\pi)^{\pm}} d\omega P(\hat{\mathbf{s}},\hat{\mathbf{s}}_0) \int_{(2\pi)^{+}} d\omega' I_d(\mathbf{r},\hat{\mathbf{s}}') \\
&\quad + \frac{\sigma_s}{4\pi}\int_{(2\pi)^{\pm}} d\omega\, P(\hat{\mathbf{s}},-\hat{\mathbf{s}}_0) \int_{(2\pi)^{-}} d\omega'\, I_d(\mathbf{r},\hat{\mathbf{s}}') \\
&= \sigma_s^{\pm} U_d^{+} + \sigma_s^{\mp} U_d^{-}.
\end{aligned} \quad (9)$$

Substituting (9) in (5) and (6), we have

$$\nabla\cdot\mathbf{F}^{+} + (\sigma_m+\sigma_e) U_d^{+} = \sigma_s^{+} U_d^{+} + \sigma_s^{-} U_d^{-} + \sigma_s^{+} I_0(z,\boldsymbol{\varrho})\exp(-\tau) \quad (10)$$

$$\nabla\cdot\mathbf{F}^{-} + (\sigma_m+\sigma_e) U_d^{-} = \sigma_s^{-} U_d^{+} + \sigma_s^{+} U_d^{-} + \sigma_s^{-} I_0(z,\boldsymbol{\varrho})\exp(-\tau). \quad (11)$$

The flux vectors $\mathbf{F}^{\pm}$ are broken into orthogonal components parallel and perpendicular to the direction $\hat{\mathbf{s}}_0$ of the incident beam as follows:

$$\mathbf{F}^{\pm} = \hat{\mathbf{s}}_0 F_p^{\pm} + \hat{\mathbf{t}} F_{\varrho}^{\pm}, \quad (12)$$

where $\hat{\mathbf{t}}$ is the unit radial vector in the plane normal to $\hat{\mathbf{s}}_0$ and

$$F_p^{\pm} = \int_{(2\pi)^{\pm}} d\omega\, I_d(\mathbf{r}, \hat{\mathbf{s}})\, \hat{\mathbf{s}} \cdot (\pm \hat{\mathbf{s}}_0), \tag{13}$$

$$F_\varrho^{\pm} = \int_{(2\pi)^{\pm}} d\omega\, I_d(\mathbf{r}, \hat{\mathbf{s}})\, \hat{\mathbf{s}} \cdot \hat{\mathbf{t}}. \tag{14}$$

By virtue of our first hypothesis on $I_d(\mathbf{r}, \hat{\mathbf{s}})$ being peaked in the $\pm \hat{\mathbf{s}}_0$ directions, we can further approximate

$$F_p^{\pm} \cong \int_{(2\pi)^{\pm}} d\omega\, I_d(\mathbf{r}, \hat{\mathbf{s}}) \cos \begin{pmatrix} 0 \\ \pi \end{pmatrix} = \pm U_d^{\pm}. \tag{15}$$

Equations (10) and (11) thus become

$$\frac{\partial}{\partial z} U_d^+ + \nabla \cdot (\hat{\mathbf{t}} F_\varrho^+) + (\sigma_m + \sigma_e)\, U_d^+ = \sigma_s^+ U_d^+ + \sigma_s^- U_d^- + \sigma_s^+ I_0(z, \varrho) \exp(-\tau), \tag{16}$$

$$-\frac{\partial}{\partial z} U_d^- + \nabla \cdot (\hat{\mathbf{t}} F_\varrho^-) + (\sigma_m + \sigma_e)\, U_d^- = \sigma_s^- U_d^+ + \sigma_s^+ U_d^- + \sigma_s^- I_0(z, \varrho) \exp(-\tau), \tag{17}$$

where z is the coordinate along $\hat{\mathbf{s}}_0$ and ϱ the radial coordinate along $\hat{\mathbf{t}}$.

Equations (16) and (17) contain too many unknowns to form a closed set, namely the transverse fluxes $\hat{\mathbf{t}} F_\varrho^{\pm}$ that are responsible for the lateral spreading of the scattered radiation. If we were to apply indiscriminately the first hypothesis to the definition of $F_\varrho^{\pm}$, the dot product $\hat{\mathbf{s}} \cdot \hat{\mathbf{t}}$ would vanish in (14) giving no lateral flux. This cannot be for obvious physical reasons. Although, by virtue of the first hypothesis, the flux components $F_\varrho^{\pm}$ are indeed small, they are differentiated with respect to the transverse coordinates in (16) and (17). In the beam geometry of interest here, the transverse scale is much smaller than the longitudinal scale and the term $\nabla \cdot \hat{\mathbf{t}} F_\varrho^{\pm}$ cannot be neglected. To model this term and close the governing set of equations, we make the following approximation which constitutes our second model hypothesis. By analogy with the modeling of turbulent transport of heat and momentum in turbulent shear flows, we assume that the transverse fluxes can be represented by a diffusion process governed by the equations

$$\hat{\mathbf{t}} F_\varrho^{\pm} = D^{\pm} \nabla_\varrho U_d^{\pm}, \tag{18}$$

where ∇_ϱ is the gradient operator in the plane normal to $\hat{\mathbf{s}}_0$. The diffusion coefficients $D^{\pm}$ are derived not from first principles but from a phenomenological representation of the random process giving rise to the lateral transport. In this framework, the diffusion coefficients are proportional to the product of the mean free path between the individual events contributing to the lateral transport of $U_d^{\pm}$ times the magnitude of the microscopic random "motion". In our case, the mean free path is proportional to the distance traveled since the photons add to form the intensities $U_d^{\pm}$ without interacting, and the strength of the random "motion" is the number of scattering events. The details of the derivation are given in [2]. The results for the diffusion coefficients at z given radiation first scattered at z' are

$$D^+(z-z') = C^+ \left[(z-z')\, S^+(z') + \int_{z'}^{z} dz'' \int_{\eta'}^{\eta''} d\eta'''\, S^+(z'') \times \exp(\eta''' - \eta') \right], \tag{19}$$

$$D^-(z-z') = C^- [(z'-z)\, S^-(z')] + C^+ \int_{z}^{z'} dz'' \int_{\eta'}^{\eta''} d\eta'''\, S^+(z'') \exp(\eta' - \eta'''), \tag{20}$$

where

$$\eta = \int dz\, \sigma_s^+(z), \tag{21}$$

$$S^+(z) = \int_0^{\pi/2} P(z, \theta) \sin\theta\, d\theta \Big/ \int_0^{\pi/2} P(z, \theta)\, d\theta, \tag{22}$$

$$S^-(z) = \int_{\pi/2}^{\pi} P(z, \theta) \sin\theta\, d\theta \Big/ \int_{\pi/2}^{\pi} P(z, \theta)\, d\theta. \tag{23}$$

In deriving $D^{\pm}$, we have assumed azimuthal symmetry for the phase function P, cylindrical symmetry for the average intensities $U_d^{\pm}$, and homogeneity in the transverse plane over the range of radial displacements for which our first hypothesis or paraxial approximation is valid. $C^{\pm}$ are empirical proportionality constants. C^- was determined by requiring the backscatter solution to tend to the single scattering LIDAR equation in the limit of negligible multiple scattering and is given by

$$C^- = \int_{\pi/2}^{\pi} \frac{P(z, \theta)}{P(z, \pi)}\, d\theta. \tag{24}$$

C^+ was chosen by matching the solutions to laboratory measurements. Its numerical value is

$$C^+ = 0.080, \tag{25}$$

and is taken as universal, i.e., applicable to all situations without further adjustments.

Substituting (18) for the transverse fluxes in (16) and (17), we obtain a closed set of equations which constitutes the proposed model for the average forward and backward intensities, i.e.

$$\frac{\partial}{\partial z} U_d^+ + D^+ \nabla_\pi^2 U_d^+ + (\sigma_m + \sigma_a + \sigma_s^-)\, U_d^+ = \sigma_s^+ I_0(z, \varrho) \exp(-\tau) + \sigma_s^- U_d^-, \tag{26}$$

$$-\frac{\partial}{\partial z} U_d^- + D^- \nabla_\varrho^2 U_d^- + (\sigma_m + \sigma_a + \sigma_s^-)\, U_d^- = \sigma_s^- I_0(z, \varrho) \exp(-\tau) + \sigma_s^- U_d^+, \tag{27}$$

where the definition $\sigma_e = \sigma_a + \sigma_s = \sigma_a + \sigma_s^+ + \sigma_s^-$, with σ_a designating the aerosol absorption coefficient, was used

for transforming the lossy terms. The molecular absorption coefficient σ_m is assumed given, and the aerosol coefficients σ_a, $\sigma_s^{\pm}$ and $D^{\pm}$ are derivable from the aerosol single-scattering properties σ_e, σ_s and $P(z, \theta)$ also assumed given.

Equations (26) and (27) are coupled parabolic partial differential equations. For most applications, we can neglect the backscatter-to-backscatter coupling, i.e., the last term in (26), and (26) and (27) can be solved sequentially. The boundary conditions are $U_d^+(0, \varrho) = U_d^-(Z, \varrho) = U_d^{\pm}(z, \infty) = 0$, where Z is the depth of the aerosol cloud. Assuming an axisymmetric Gaussian profile for $I_0(z, \varrho)$ and using the method of the Green's function, we can write the solutions in the following general analytic form:

$$U_d^+(z, \varrho) = \frac{P_0}{\pi w_0^2} \int_0^z dz' \frac{E(z, z')}{H(z, z')} \exp\left(-\frac{\varrho^2}{w_0^2 H(z, z')}\right), \quad (28)$$

$$U_d^-(z, Z, \varrho) = \frac{P_0}{\pi w_0^2} \int_z^Z dz' \frac{G(z, z')}{K(z, z')} \exp\left(-\frac{\varrho^2}{w_0^2 K(z, z')}\right) + \frac{P_0}{\pi w_0^2} \int_z^Z dz' \int_0^{z'} dz'' \frac{L(z, z', z'')}{M(z, z', z'')} \times \exp\left(-\frac{\varrho^2}{w_0^2 M(z, z', z'')}\right), \quad (29)$$

where P_0 and w_0 are, respectively, the power and beam waist of the incident beam. The functions E, G and L are transmittance functions and H, K and M, beam spreading functions. They are given by integrals over z of functions of the aerosol absorption, scattering and diffusion coefficients as follows:

$$E(z, z') = \sigma_s^+(z')\, T(z') \exp\left[-\int_{z'}^{z} (\sigma_m + \sigma_a + \sigma_s^-)\, dz''\right], \quad (30)$$

$$G(z, z') = \sigma_s^-(z')\, T(z') \exp\left[-\int_{z}^{z'} (\sigma_m + \sigma_a + \sigma_s^-)\, dz''\right], \quad (31)$$

$$L(z, z, z''') = \sigma_s^-(z')\, \sigma_s^+(z'')\, T(z'') \times \exp\left[-\int_{z''}^{z'} (\sigma_m + \sigma_a + \sigma_s^-)\, dz'''\right] \times \exp\left[-\int_{z}^{z'} (\sigma_m + \sigma_a + \sigma_s^-)\, dz'''\right], \quad (32)$$

$$H(z, z') = W(z') + \frac{4}{w_0^2} \int_{z'}^{z} D^+(z''' - z')\, dz''', \quad (33)$$

$$K(z, z') = W(z') + \frac{4}{w_0^2} \int_{z}^{z'} D^-(z''' - z')\, dz''', \quad (34)$$

$$M(z, z', z'') = W(z'') + \frac{4}{w_0^2} \int_{z''}^{z'} D^+(z''' - z')\, dz''' + \frac{4}{w_0^2} \int_{z}^{z'} D^-(z''' - z')\, dz''', \quad (35)$$

where

$$T(z) = \exp\left[-\int_0^z (\sigma_m + \sigma_a + \sigma_s)\, dz\right], \quad (36)$$

$$W(z) = 1 + \beta^2 (z - z_w)^2 / w_0^2. \quad (37)$$

In (37), β and z_w are, respectively, the far field divergence including diffraction and the axial coordinate of the beam waist of the incident beam, both assumed given. The reduced or unscattered intensity is given by

$$U_{ri}(z, \varrho) = \frac{P_0}{w_0^2} \frac{T(z)}{W(z)} \exp\left(-\frac{\varrho^2}{w_0^2 W(z)}\right). \quad (38)$$

The functions $U_d^{\pm}$ are irradiance functions applicable to detection over 2π sr. For receivers of limited fields of view, the angular distribution of the radiation flux must be taken into account. This cannot be done exactly in the framework of the present model since the radiative-transfer equation was integrated over the solid angle. Instead, we approximate the field of view dependence by multiplying the elementary contributions to the integrals in (28) and (29) by the probabilities $\mathscr{P}_{ri}$ and $\mathscr{P}_d$ that the photons crossing the receiver aperture do so within an angular range less than or equal to the receiver field of view α as follows:

$$U_d^+(z, \varrho, \alpha) = \frac{P_0}{\pi w_0^2} \int_0^z dz'\, \mathscr{P}_{ri}(z, z', \varrho, \alpha) \frac{E(z, z')}{H(z, z')} \times \exp\left(-\frac{\varrho^2}{w_0^2 H(z, z')}\right), \quad (39)$$

$$U_d^-(z, Z, \varrho, \alpha) = \frac{P_0}{\pi w_0^2} \int_z^Z dz'\, \mathscr{P}_{ri}(z, z', \varrho, \alpha) \frac{G(z, z')}{K(z, z')} \times \exp\left(-\frac{\varrho^2}{w_0^2 K(z, z')}\right) + \frac{P_0}{\pi w_0^2} \int_z^Z dz'\, \mathscr{P}_d(z, z', \varrho, \alpha) \int_0^{z'} dz'' \times \frac{L(z, z', z'')}{M(z, z', z'')} \times \exp\left(-\frac{\varrho^2}{w_0^2 M(z, z', z'')}\right). \quad (40)$$

The probabilities $\mathscr{P}_{ri}$ and $\mathscr{P}_d$ are estimated from the distribution of the random paths of the photons scattered from the reduced and scattered intensity beams $U_{ri}(z, \varrho)$ and $U_d^+(z, \varrho)$, respectively. They are functions of the medium scattering coefficient and angular phase function. The derivation steps and approximations are discussed at length in [2]. The results are

$$\mathscr{P}_{ri}(z, z', \varrho, \alpha) \cong \exp\left(-\int_{z'}^{z} \sigma_s^+\, dz''\right) \mathscr{R}_1(z, z', \varrho, \alpha) + \left[1 - \exp\left(-\int_{z'}^{z} \sigma_s^+\, dz''\right)\right] \times \frac{1}{(z - z')} \int_{z'}^{z} dz''\, \mathscr{R}_2(z, z', z'', \varrho, \alpha), \quad (41)$$

where

$$\mathscr{R}_1(z, z', \varrho, \alpha) = \frac{\int d^2\varrho' U_{ri}(z', \varrho') P(z', \theta_1) R(\theta_1; \alpha)}{\int d^2\varrho' U_{ri}(z', \varrho') P(z', \theta_1)}, \quad (42)$$

$$\mathscr{R}_2(z, z', z'', \varrho, \alpha) = \frac{\int d^2\varrho' \int d^2\varrho'' U_{ri}(z', \varrho') P(z', \theta_2) P(z'', \theta_3) R(\theta_4; \alpha)}{\int d^2\varrho' \int d^2\varrho'' U_{ri}(z', \varrho') P(z', \theta_2) P(z'', \theta_3)}. \quad (43)$$

In (42) and (43), $R(\theta; \alpha)$ is the receiver angular aperture profile of width α and the angles θ_i are related to the other variables as follows:

$$\cos\theta_1 = \frac{z - z'}{[(z-z')^2 + |\varrho - \varrho'|^2]^{1/2}}, \quad (44)$$

$$\cos\theta_2 = \frac{z'' - z'}{[(z''-z')^2 + |\varrho'' - \varrho'|^2]^{1/2}}, \quad (45)$$

$$\cos\theta_3 = \frac{(z''-z')(z-z'') + (\varrho''-\varrho')\cdot(\varrho-\varrho'')}{[(z''-z')^2 + |\varrho''-\varrho'|^2]^{1/2}[(z-z'')^2 + |\varrho-\varrho''|^2]^{1/2}}, \quad (46)$$

$$\cos\theta_4 = \frac{z - z''}{[(z-z'')^2 + |\varrho - \varrho''|^2]^{1/2}}. \quad (47)$$

The function $\mathscr{P}_d(z, z', \varrho, \alpha)$ is obtained by substituting $U_d^+(z', \varrho')$ for $U_{ri}(z', \varrho')$ in the expressions for $\mathscr{R}_1$ and $\mathscr{R}_2$.

The solution method is as follows. The functions $U_d^+(z, \varrho)$ and $U_{ri}(z, \varrho)$ are first calculated with (28) and (38). The probabilities functions $\mathscr{P}_{ri}$ and $\mathscr{R}_d$ are then obtained by substitution of the solutions for $U_{ri}(z, \varrho)$ and $U_d^+(z, \varrho)$ in (41–43). Finally, the forward and backward average intensities $U_d^+(z, \varrho, \alpha)$ and $U_d^-(z, Z, \varrho, \alpha)$ for the required receiver geometry are calculated by integrating (39) and (40). The necessary inputs are the receiver field of view function $R(\theta, \alpha)$, the molecular absorption coefficient σ_m of the medium, and the aerosol single scattering phase function P and extinction and scattering coefficient σ_e and σ_s. The remaining scattering and diffusion coefficients $\sigma_s^{\pm}$ and $D^{\pm}$ are calculated by substitution in (8), (19) and (20).

The LIDAR backscatter signal $\mathscr{L}(Z, z_0, \alpha)$ from range Z for a receiver position z_0 on the beam axis ($\varrho = 0$), and field of view α is obtained by differentiating U_d^- with respect to Z, i.e.,

$$\mathscr{L}(z_0, Z, \alpha) = \frac{d}{dZ} U_d^-(z_0, Z, 0, \alpha) = \frac{P_0}{\pi w_0^2}\left\{\mathscr{P}_{ri}(z_0, Z, 0, \alpha)\frac{G(z_0, Z)}{K(z_0, Z)} + \mathscr{P}_d(z_0, Z, 0, \alpha)\int_0^Z dz''\frac{L(z_0, Z, z'')}{M(z_0, Z, z'')}\right\}. \quad (48)$$

$\mathscr{L}(z_0, Z, \alpha)$ is the backscatter return per unit spatial resolution length and per unit aperture area for a continuous wave beam. To calculate the return for a more conventional pulsed beam, P_0 must be replaced by the pulse energy divided by the pulse duration $\mathscr{T}$, and the solution $\mathscr{L}$ of (48) must be multiplied by the receiver aperture area and the spatial resolution $c\mathscr{T}/2$, where c is the speed of light.

To transform time-after-pulse into range, the pulse stretching created by multiple scattering must be negligible. This is generally the case for ground-based applications. Because the fields of view are small, most scattering events contributing to the measured LIDAR signal are in the near forward direction except for one backscattering. Moreover, since the optical depth does not exceed 3–4, there are only 6–8 such scatterings and, since they occur at small angles, they produce little difference in the length of the path traveled by the photons. Under these conditions of small fields of view, small optical depths and relatively short ranges of ground-based systems, the photons that wander off-axis to cause significant path differences while still being detected by the LIDAR receiver have to experience at least 2 scatterings at angles close to 90° in addition to the backscattering near 180°. Because the phase function of most natural aerosols is peaked in the forward direction at visible and infrared LIDAR wavelengths, the photon paths with such large-angle scatterings are orders of magnitude less probable than the multiple-forward-scattering paths described above. Hence, for practical ground-based atmospheric applications, there is no significant blurring of the range resolution on the scale of typical pulse widths of 10–30 ns, and (48) is applicable to pulsed LIDAR.

2 Experimental results

2.1 Medium-scale laboratory simulation

Transmission and backscatter measurements were performed in a laboratory simulation experiment described

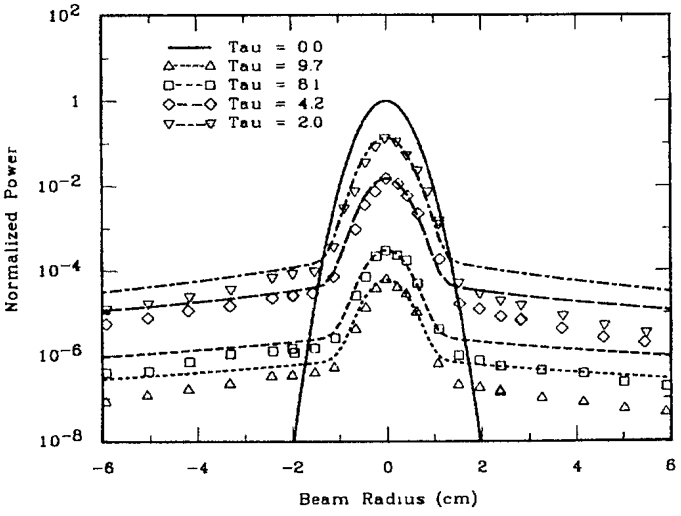

Fig. 2. Profiles of a 1.06 μm beam measured at the exit plane of a 3.2 m long chamber filled with a homogeneous water droplet aerosol of different concentrations. The concentrations are given in terms of total cloud optical depths (Tau). The receiver field of view was 140 mrad. The *symbols* represent the measurements and the *curves* the solutions calculated with the model of this paper

in [3]. Water droplet clouds of adjustable concentrations were produced in a closed chamber 3.2 m long, 1 m wide and 0.75 m high. The source was a 1.06 μm modulated and collimated laser beam directed along the main axis of the chamber. The extinction coefficient at the source wavelength was adjustable between 0.25–7 m^{-1}.

Figure 2 is a plot of transmitted beam profiles obtained at different optical depths τ for a constant field of view of 140 mrad. The profiles were measured by scanning a 1 mm diameter receiver at the exit plane of the chamber. Two main features can be observed from Fig. 2. On the one hand, the central portion of the transmitted beam conserves its Gaussian shape, is virtually unaffected by multiple scattering and its on-axis beam intensity follows very closely the single-scattering fading law of exp $(-\tau)$. On the other hand, this narrow central portion is surrounded by a wide aureole which is due to multiple forward scattering and increases with optical depth relative to the on-axis intensity. The fit between these measurements and the model calculations is quite good over the full parameter range despite the asymmetry in the data caused by a slight tilt of the receiver axis with respect to the incident beam. These quantitative results are also in good agreement with the qualitative picture of Fig. 1.

The effect of the receiver field of view on measured profiles is shown in Fig. 3. In this case, the profiles were recorded at about the same optical depth but for different fields of view of 20, 140 and 350 mrad. The central core is nearly independent of the field of view since it is made up in the most part of the unscattered beam. The off-axis aureole grows rapidly with increasing field of view but eventually levels off as indicated by the smaller difference between 140 and 350 mrad than between 20 and 140 mrad. Again, the calculated profiles fit the experimental data very well.

In addition to the transmitted profiles, the cloud-integrated backscatter, or the backscatter from the length of the chamber, was also measured. For this, a 5 cm aperture receiver was placed close to the laser axis at a distance of 11.2 m in front of the chamber. The chamber was divided into three sections of equal length, separated by specially designed air screens, in which different cloud concentrations could be produced and maintained. The cloud structure obtained in this manner is designated by a three-digit code that gives the relative concentration in each section. For example, a 1-2-3 cloud has a concentration twice and three times as large in the second and third section than in the first, respectively. The measurements and corresponding model solutions are plotted in Fig. 4 for various cloud structures as functions of total cloud optical depth. The agreement is very good. As can be seen, the backscatter depends strongly on the structure; for the same total optical depth, clouds that are denser in the front section produce greater returns. Also drawn in Fig. 4 are the single-scattering solutions calculated by integrating the conventional single-scattering LIDAR equation. They saturate for optical depths greater than ≈ 2 at a level significantly below the measurements. Clearly, multiple scattering contributes a large fraction of the backscatter returns and greatly enhances the differences due to spatial structure. Figure 4 shows that these effects are accurately taken into account by our model solutions.

By use of large rotating chopping blades and synchronous detection, the backscatter returns from individual cloud sections could be singled out with reasonable accuracy. This was done to simulate, however crudely, range-resolved LIDAR measurements. Sample results are plotted in Figs. 5 and 6 for a receiver field of view of 3 and 15 mrad, respectively. As in Fig. 4, the abscissa in the plots of Figs. 5 and 6 is the total cloud optical depth. Despite the experimental scatter, especially at small optical depths, the agreement between the measured data and

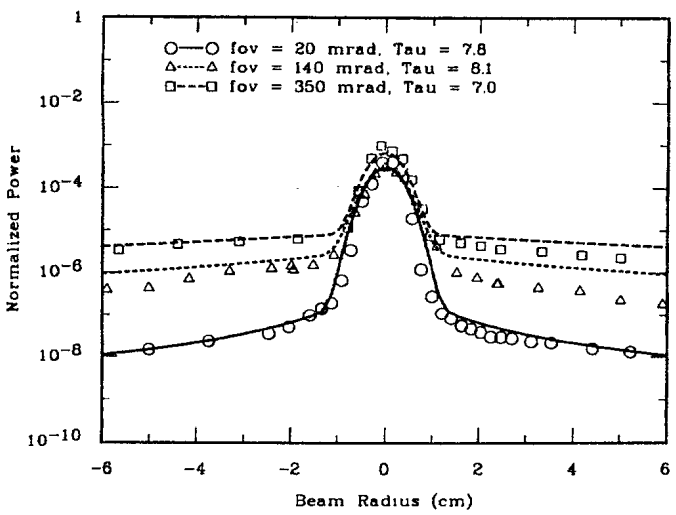

Fig. 3. Transmitted profiles as in Fig. 2 but for different receiver fields of view. The cloud length was 2.6 m for the 20 and 350 mrad results and 3.2 m for the 140 mrad results

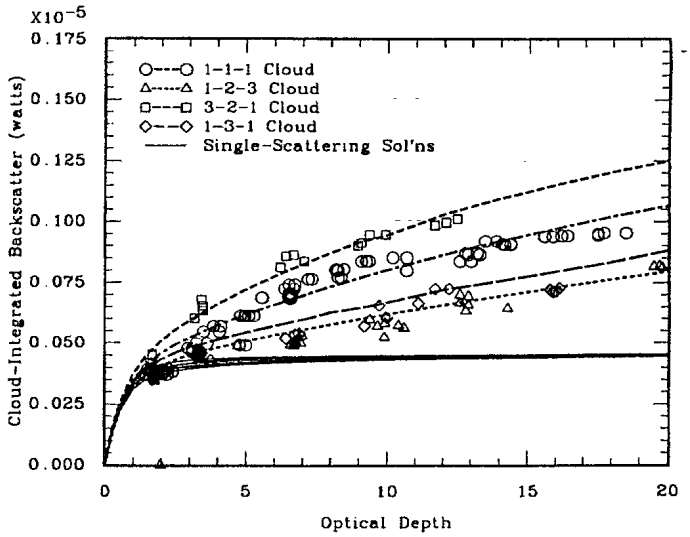

Fig. 4. Cloud integrated backscatter returns at 1.06 μm as functions of the cloud total optical depth for different spatial structures of the water droplet aerosol contained in the same chamber as for the results of Figs. 2 and 3. The *symbols* represent the measurements and the *curve*, the solutions calculated with the model of this paper. The *thin-line curves* are the corresponding single-scattering solutions

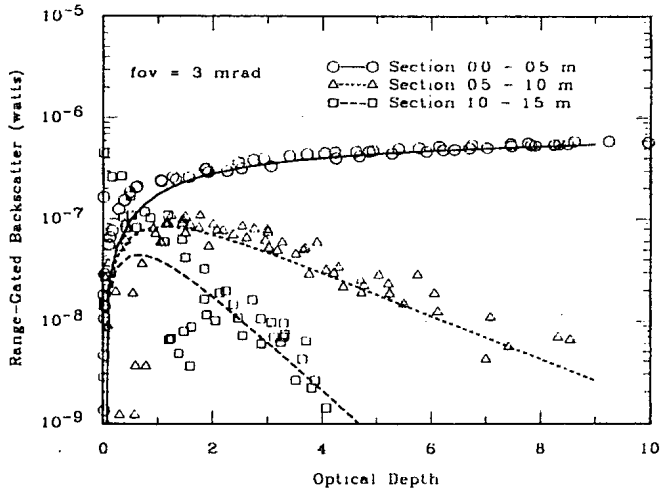

Fig. 5. Backscatter returns from different sections of the cloud chamber for a receiver field of view of 3 mrad in the case of a homogeneous aerosol. The *symbols* represent the measurements and the *curves* the solutions calculated with the model of this paper

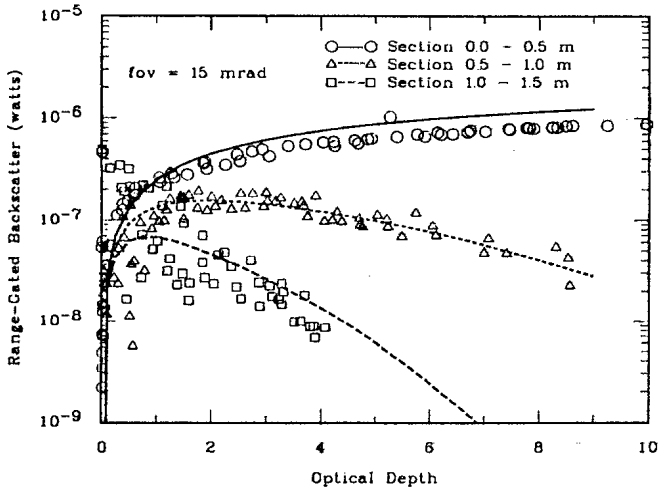

Fig. 6. Same as Fig. 5 except for a receiver field of view of 15 mrad

the model calculations is quite good. The only systematic discrepancy is for the return from Sec. 1 at 15 mrad where the calculations are greater by about 50%. However, this is small compared with the differences between the cloud sections which are well predicted by the solutions, both in magnitude and dependence on optical depth. The measurement errors could not be estimated with confidence in this case.

2.2 *Small-scale* LIDAR *simulation*

An elegant laboratory simulation of LIDAR measurements was carried ont by a group of the University of Florence [5]. They were able to achieve a range resolution small enough for the laboratory scale by using a 766.5 nm laser source with a short pulse length of 4 ps. The scattering medium consisted of a water suspension of polystyrene spherical particles of known concentration and size distribution contained in a cylindrical cell. The cell length and diameter were respectively 100 and 80 mm.The 4 ps pulse duration gives a spatial resolution $c\mathcal{T}/2$ in water equal to 0.45 mm but this was degraded to 2.8 mm because of the 25 ps response time of the streak camera recording system. The range-resolved backscatter signals were measured at 250 mm in front of the cell near the laser axis with a receiver of aperture diameter and field of view (full angle) equal to 0.2 mm and 12.2 mrad, respectively. Measurements were made of both parallel and perpendicular polarization states. For the present comparisons, the polarization components were added because our calculation model does not handle polarization. Four different particle size distributions were used and, in each case, the concentrations were adjusted to give scattering extinctions ranging from 0.006 to 0.13 mm^{-1}.

Typical comparison results are plotted in Figs. 7 and 8 for particle suspensions of approximately the same extinction coefficient near 0.065 mm^{-1} but for different average particle diameters, 5.4 μm in Fig. 7 and 0.09 μm in Fig. 8. The experimental data were reported in relative units and have been adjusted for a perfect match at zero range. Also shown in Figs. 7 and 8 are the corresponding single-scattering solutions. As can be seen, the multiple-scattering contributions are significant for the large particles, about 20 times the single-scattering predictions at a range of 50 mm, but almost negligible for the small particles. The calculated solutions agree very well with these observations except that they overestimate by ≈50% the multiple-scattering contributions in the case of large particles. Other comparisons for different extinction coefficients and particle sizes show a level of agreement similar to or better than that illustrated by the examples of Figs. 7 and 8. Overall, the model perforances are quite

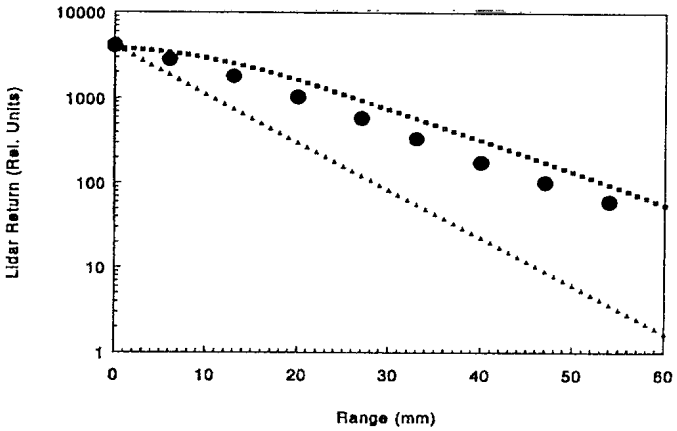

Fig. 7. Range-resolved simulated LIDAR returns at 766.5 nm (wavelength in air) from a 100 mm long cell containing a suspension of spherical polystyrene particles in water for a 12.2 mrad (*full angle*) field of view receiver located 250 mm in front of the cell. The particulate extinction coefficient was 0.063 mm^{-1} and the average particle diameter, 5.4 μm. The *small squares* are the multiple-scattering solution calculated with the model of this paper, the *small triangles* the single-scattering solution, and the *large solid circles* the measurements

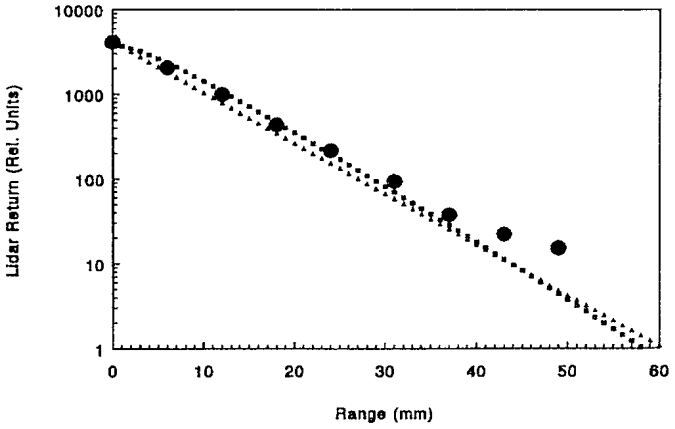

Fig. 8. Same as Fig. 7 except for an extinction coefficient of 0.067 mm^{-1} and an average particle diameter of 0.09 μm

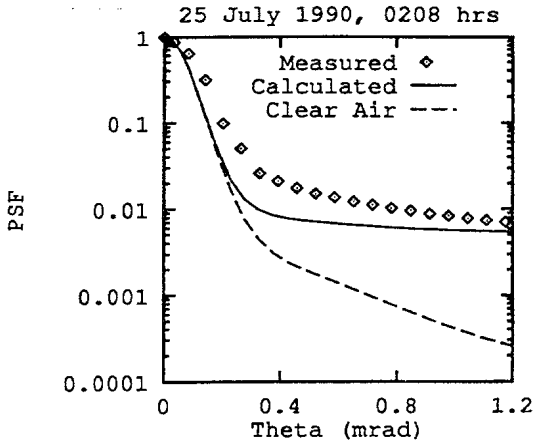

Fig. 9. Visible point-spread function measured in advection fog for a range and extinction coefficient of 530 m and 8.42 km^{-1}, respectively. The *symbols* represent the measurements, the *continuous line curve* the solution calculated with the model of this paper, and the *dashed line curve* the clear-air function

satisfactory. Differences of 50% may seen large but they do not necessarily give the limits of the model since all the experimental parameters cannot be reproduced exactly. For example, the calculation model requires a Gaussian field of view profile; the e^{-1} width was chosen equal to the experimental value but the true profile is closer to a top-hat than a Gaussian function.

2.3 Imaging experiment in the atmosphere

The experiments discussed in the preceding sections were performed on a laboratory scale of a few m in the first case and a few tens of mm in the second case. We report here on an imaging measurements carried out in the atmosphere on a scale of the order of 1 km. The experiment described at length in [4] consisted in imaging visible point sources located, respectively, at 530 and 920 m. Images of the point sources, or point spread functions, were recorded under conditions of reduced visibility created by haze, fog and rain. The point sources were 90 mm in diameter, 10° divergence visible beams from 1000 W quartz halogen lamps. The atmospheric haze, fog and rainfall properties were monitored by a transmissometer aligned along the imaging axis, by two visibility meters, one near the camera and one near the 530 m source, and by particle and raindrop size distribution sensors located near the camera. These provided the necessary inputs to carry out the calculation of the point-spread functions under the assumption of homogeneity along the path between the sources and the camera.

Examples of measured and calculated point spread functions for a large particle advection fog are plotted in Figs. 9 and 10. The shape of the point-spread image profile is very characteristic: a central peak surrounded by a wide aureole formed by aerosol scattered light. For the cases illustrated, the aureole is quite intense and shows a slope much less than for the clear air profile. The model solutions fit the measurements very well: both the magnitude and slope of the aureole are well predicted for both sources.

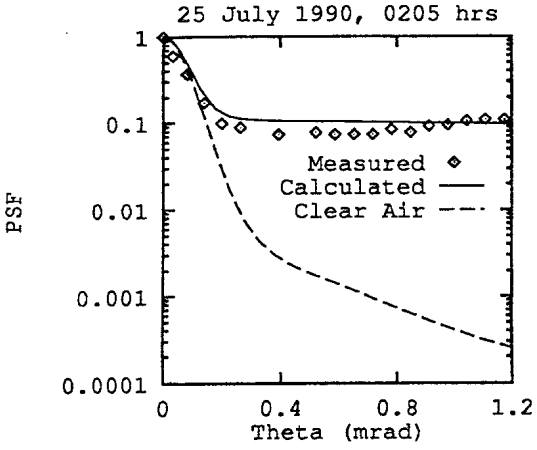

Fig. 10. Same as Fig. 9 except for a range of 920 m and an extinction coefficient of 9.34 km^{-1}

3 Conclusion

A multiple-scattering propagation model for the solution of the forward- and backscattered intensity profiles of narrow light beams in aerosol media is described. The two main model hypotheses are the paraxial approximation and the representation of the lateral transport of the scattered intensity by a diffusion process. The model requires two empirical constants determined by comparisons with measured data for one, and by requiring that the backscatter solution tend to the single-scattering LIDAR equation in the limit of negligible multiple scattering for the other. The resulting constants are not adjustable. The necessary inputs are the characteristics of the source beam, the molecular absorption coefficient of the medium, and the single scattering aerosol extinction and scattering coefficients and angular phase function. The model can handle inhomogeneities along the incident beam axis. The solutions are obtained in general

analytic form and require very modest computer resources.

The model solutions were compared with forward- and backscatter measurements performed in the laboratory on scales of a few tens of mm to a few m, and in the atmosphere on a scale of 1 km. The agreement is very satisfactory. The influences of source-receiver-cloud geometry, cloud spatial structure, optical depth, particle size, and receiver field of view are well reproduced by the solutions. Based on these comparisons, it is concluded that the model is valid for optical depth up to ≈ 10, for phase functions corresponding to average size parameters of order 1 and greater, and for off-axis positions not exceeding $\approx 25\%$ of the scattering length σ_s^{-1}.

Acknowledgements. The photograph of Fig. 1 is the work of D. Hutt. The measurements reported in Sect. 2.1 were carried out under contract at Optech Inc., Toronto, Canada by B. Smith. I am indepted to G. Zaccanti and P. Bruscaglioni of the University of Florence for providing the experimental data of Sect. 2.2. The aerosol properties needed for the calculations of Sect. 2.3 were recorded, validated and supplied to us by G. Koenig and V. Turner of Air Force Phillips Laboratory and G. Trusty of Naval Research Laboratory. I am grateful to B. Enns, J. Oman and L. Durand for their able technical assistance.

References

1. L.R. Bissonnette, P. Bruscaglioni, A. Ismaelli, G. Zaccanti, A. Cohen, Y. Benayahu, R.D. Haracz, L.D. Cohen, C. Flesia, P. Schwendimann, M. Oppel, D.M. Winkel, E.P. Zege, I.L. Katsev, I.N. Polonsky: Appl. Phys. B **60**, 355 (1995)
2. L.R. Bissonnette: Appl. Opt. **27**, 2478 (1988)
3. L.R. Bissonnette, R.B. Smith, A. Ulitsky, J.D. Houston, A.I. Carswell: Appl. Opt. **27**, 2485 (1988)
4. L.R. Bissonnette: Opt. Eng. **31**, 1045 (1992)
5. G. Zaccanti, P. Bruscaglioni, M. Gurioli, P. Sansoni: Appl. Opt. **32**, 1590 (1993)

#152221

NO. OF COPIES NOMBRE DE COPIES	COPY NO. COPIE N°	INFORMATION SCIENTIST'S INITIALS INITIALES DE L'AGENT D'INFORMATION SCIENTIFIQUE
1	1	JC
AQUISITION ROUTE ▶ FOURNI PAR	DREV	
DATE ▶	19 Jun 91	
DSIS ACCESSION NO. ▶ NUMÉRO DSIS	95-03119	

DND 1158 (6-87)

National Defence / Défense nationale

PLEASE RETURN THIS DOCUMENT TO THE FOLLOWING ADDRESS:

DIRECTOR
SCIENTIFIC INFORMATION SERVICES
NATIONAL DEFENCE
HEADQUARTERS
OTTAWA, ONT. - CANADA K1A 0K2

PRIÈRE DE RETOURNER CE DOCUMENT À L'ADRESSE SUIVANTE:

DIRECTEUR
SERVICES D'INFORMATION SCIENTIFIQUES
QUARTIER GÉNÉRAL
DE LA DÉFENSE NATIONALE
OTTAWA, ONT. - CANADA K1A 0K2